Interaction between a simplified soft palate and compressible viscous flow

Mohammadtaghi Khalili[a,*], Martin Larsson[b], Bernhard Müller[a]

[a]*Department of Energy and Process Engineering, Norwegian University of Science and Technology (NTNU), Kolbjørn Hejes vei 2, NO-7491 Trondheim, Norway*
[b]*SINTEF Materials and Chemistry, S. P. Andersens vei 15B, Trondheim, Norway*

Abstract

Fluid–structure interaction in a simplified 2D model of the upper airways is simulated to study flow–induced oscillation of the soft palate in the pharynx. The goal of our research has been a better understanding of the mechanisms of the Obstructive Sleep Apnea Syndrome and snoring by taking into account compressible viscous flow. The inspiratory airflow is described by the 2D compressible Navier–Stokes equations, and the soft palate is modeled as a flexible plate by the linearized Euler–Bernoulli thin beam theory. Fluid–structure interaction is handled by the arbitrary Lagrangian–Eulerian formulation. The fluid flow is computed by utilizing 4^{th} order accurate summation by parts difference operators and the 4^{th} order accurate classical Runge–Kutta method which lead to very accurate simulation results. The motion of the cantilevered plate is solved numerically by employing the Newmark time integration method. The numerical schemes for the structure are verified by comparing the computed frequencies of plate oscillation with the associated second mode eigenfrequency in vacuum. Vortex dynamics is assessed for the coupled fluid-structure system when both airways are open and when one airway is closed. The effect of mass ratio, rigidity and damping coefficient of the plate on the oscillatory behaviour is investigated. An acoustic analysis is carried out to characterize the acoustic wave propagation induced by the plate oscillation. It is observed that the acoustic wave corresponding to the quarter wave mode along the length of the duct is the dominant frequency. However, the frequency of the plate oscillation is recognizable in the acoustic pressure when reducing the amplitude of the quarter wave mode.

Keywords: Fluid-structure interaction (FSI); High order finite difference method; Cantilevered flexible plate; Acoustics; Obstructive sleep apnea syndrome (OSAS)

1. Introduction

Fluid structure interaction (FSI) refers to a phenomenon where a flow field interacts with compliant or elastic structures. The behaviour of many dynamic systems is influenced by the interaction between the fluid flow and structural components that are involved in the system. This interaction happens in a wide range of phenomena such as flapping of insect wings, the flutter of flags, the vibration of bridges and structures and the aeroelasticity of aircraft wings. With growing interest in the multidisciplinary field of biomedical and biomechanical engineering, a vast amount

*Corresponding author
Email address: mohammadtaghi.khalili@ntnu.no (Mohammadtaghi Khalili)

of research has been conducted to comprehend fluid-structure interaction in physiological systems in the human body (Tian et al., 2014; Wu and Cai, 2014; Larsson and Müller, 2012).

One of the prime examples of FSI in biomechanical systems is the dynamics of the upper airways where the interaction between inspiratory and expiratory airflow with soft tissues may lead to flow-induced instabilities. Disorders of the upper airways are often associated with respiratory syndromes. Among these, obstructive sleep apnea (OSA) and snoring are closely related to the flow conditions in the upper airways. Obstructive sleep apnea syndrome (OSAS) is one of the most prevalent types of sleep-disordered breathing caused by repetitive collapse of the soft tissues in the upper airways. Estimates show that OSAS affects 2–4% of the adult population (Young et al., 1993). The significant consequence of OSAS is sleep fragmentation which can lead to increased daytime sleepiness, fatigue-related accidents and risk of cardiovascular diseases (Malhotra and White, 2002). Even though snoring does not necessarily mean that one has sleep apnea, estimates show that 10% of snorers are at risk of OSAS (Bertram, 2008).

In recent years, the fluid flow over a cantilevered plate has been a reliable theoretical model not only for many engineering applications but also for many biomechanical systems like human palatal snoring (Kuhl and DesJardin, 2012; Huang and Zhang, 2013). Computational models have been increasingly employed to model upper airways. In most of the investigations, inviscid flow has been assumed to develop numerical models for flow-induced instabilities (Guo and Païdoussis, 2000; Howell et al., 2009; Shoele and Mittal, 2016). A cantilevered beam immersed in a channel flow has been investigated by Auregan and Depollier (1995) both analytically and experimentally to understand snoring. They employed linear small deflection beam theory and neglected frictional losses. Quasi-parallel flow was assumed and the pressure on the beam was estimated by mass conservation and the Bernoulli equation. Huang (1995) modeled a cantilevered elastic plate immersed in an axial flow, and also conducted wind tunnel experiments to verify theoretical results for palatal snoring. The governing equation for linear plate bending was solved by using finite expansion of orthogonal in vacuum modes. Although the viscous effect of circulation was implicitly imposed by the Kutta–Joukowski condition at the free trailing edge of the plate, viscosity was neglected and potential flow theory was used. He found that fluid loading resulting from the interaction of the wake vortices is responsible for the irreversible energy transfer in the flow–induced instability.

Linear instability of thin elastic plates with different leading and trailing edge conditions in 2D channel flow was investigated by Guo and Païdoussis (2000). Similar to the work done by Auregan and Depollier (1995), the 1D linear plate equation was solved by applying the Galerkin method where plate deflections were recast in the form of an expansion series of orthogonal beam functions. A Fourier transform technique was applied to solve the perturbation pressure from the potential flow equations. They found that single-mode and coupled-mode flutter are dominant modes for plates with a free trailing edge and free-free edge, respectively. However, the instability of plates with either clamped or pinned boundary condition at edges may occur through first-mode divergence exceeding other types of instability modes (Guo and Païdoussis, 2000).

Tang and Païdoussis (2007, 2008) performed computational investigations of non-linear large deflection of cantilever plates using the inextensibility condition surrounded by axial flow. The flow was assumed purely inviscid even if a separate viscous drag was coupled into the plate equation, and the imposed pressure difference on the plate was estimated using an unsteady lumped vortex model. Their analytical results show that if critical flutter velocity and frequency increase, the drag coefficient will increase. Furthermore, in experimental results they observed sudden flutter vibration at critical velocities. However, the onset of oscillation will be more unlikely, if the flow

velocity is reduced from an initial plate flutter. They demonstrated the possibility of a hysteresis phenomenon by including an unsteady von Kármán vortex street in their simulation. Conducting more theoretical investigations on the effect of trailing edge wakes on plate instability, they concluded that longer plates together with higher critical frequencies cause higher ratios of plate vibration velocity to wake-induced flow velocity, and thus a smaller effect of wake-induced flow velocities on the plate.

In contrast to the studies mentioned above, Balint and Lucey (2005) and Tetlow and Lucey (2009) included viscous effects directly in their instability analysis by solving the Navier–Stokes equation in a 2D channel surrounding a cantilever plate. Whereas Balint and Lucey (2005) modeled the motion of a thin plate using linear plate theory under differential pressure, Tetlow and Lucey (2009), added a tension term defined as the skin friction force acting on both the upper and lower sides of the plate. In both studies, the finite element method was employed in order to solve the unsteady, laminar Navier–Stokes equations in a channel geometry with inlet boundaries above and below the flexible plate and to estimate fluid loads interfacing with the plate. Their fluid solver was explicitly coupled to the structural finite difference solver. Based on their numerical results, when both upper and lower inlets are open, a flutter-type instability is initiated at a critical Reynolds number, while if one of the inlets is closed, a divergence-type instability occurs at a critical velocity. Although Tetlow and Lucey (2009) imposed a constant pressure drop along the channel rather than assuming velocity-driven flow, flutter instabilities similar to those found by Balint and Lucey (2005) were observed.

In this paper, we use a compressible viscous flow model to simulate the flow-induced oscillation of the soft palate in the pharynx by a simplified 2D model (cf. Fig.1). We couple the compressible flow in the pharynx to a cantilevered thin plate model of the soft palate in an arbitrary Lagrangian-Eulerian (ALE) formulation by using a two-way explicit coupling. A high order finite difference method based on summation by parts (SBP) (Strand, 1994; Svärd and Nordström, 2014) is used for the spatial discretization of the compressible Navier–Stokes equations. The classical fourth order explicit Runge–Kutta scheme is applied for time integration for the sake of accuracy and easy parallelization. The Newmark time integration method and central finite difference method are used to solve the linearized Euler–Bernoulli thin beam model. To achieve geometric flexibility with high order operators for this simplified model in the upper airways, the multi block structured grid approach is employed. We investigate the effect of material properties on the oscillation behaviour of the flexible plate. Using compressible fluid flow permits us to investigate the acoustic waves inside the channel and also the effect of flexible plate oscillation on sound generation.

The paper is organized as follows. In Section 2, the models for fluid flow, structure and their coupling by FSI are presented. In Section 3, first the verification of the structure scheme is performed. Next, the numerical simulation of the plate oscillation for flow with artificially increased Mach numbers up to 0.02 and Reynolds numbers up to 756 is presented. Then, the effects of plate properties on the plate oscillation induced by the flow are examined, and finally the results of the acoustic analysis are shown. Conclusions are stated in Section 4.

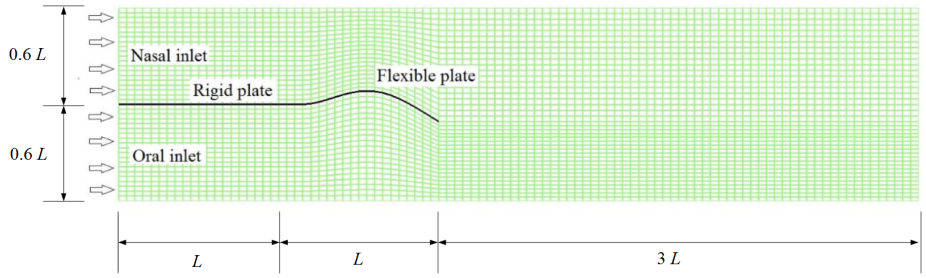

(a) Schematic of the computational model

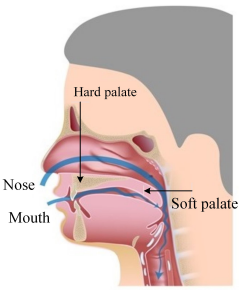

(b) The anatomy of upper airways.

Figure 1: Computational model and real geometry.

2. Model

2.1. Fluid flow

In the present study, the 2D compressible Navier–Stokes equations in perturbation form are solved. The perturbation formulation is employed to minimize cancellation errors when discretizing the Navier–Stokes equations for compressible low Mach number flow (Sesterhenn et al., 1999; Müller, 2008). The conservative form of the 2D compressible Navier–Stokes equations in perturbation formulation can be written as

$$\mathbf{U}'_t + \mathbf{F}^{c\prime}{}_x + \mathbf{G}^{c\prime}{}_y = \mathbf{F}^{v\prime}{}_x + \mathbf{G}^{v\prime}{}_y \tag{1}$$

where $\mathbf{U}' = \mathbf{U} - \mathbf{U_0}$ is the vector of conservative perturbation variables with $\mathbf{U} = (\rho, \rho u, \rho v, \rho E)^T$ the vector of the conservative variables and $\mathbf{U}_0 = (\rho_0, 0, 0, (\rho E)_0)^T$ the stagnation values.

The conservative perturbation variables $\mathbf{U}'$ and the inviscid ($\mathbf{F}^{c\prime}$, $\mathbf{G}^{c\prime}$) and viscous perturbation flux vectors ($\mathbf{F}^{v\prime}$, $\mathbf{G}^{v\prime}$) are defined by $\mathbf{F}^{c\prime} = \mathbf{F}^c(\mathbf{U}) - \mathbf{F}^c(\mathbf{U_0})$, etc.

$$\mathbf{U}' = \begin{pmatrix} \rho' \\ (\rho u)' \\ (\rho v)' \\ (\rho E)' \end{pmatrix},$$

$$\mathbf{F}^{c\prime} = \begin{pmatrix} (\rho u)' \\ (\rho u)'u' + p' \\ (\rho v)'u' \\ ((\rho H)_0 + (\rho H)')u' \end{pmatrix}, \quad \mathbf{G}^{c\prime} = \begin{pmatrix} (\rho v)' \\ (\rho u)'v' \\ (\rho v)'v' + p' \\ ((\rho H)_0 + (\rho H)')v' \end{pmatrix},$$

$$\mathbf{F}^{v\prime} = \begin{pmatrix} 0 \\ \tau'_{xx} \\ \tau'_{xy} \\ u'\tau'_{xx} + v'\tau'_{xy} + \kappa T'_x \end{pmatrix}, \quad \mathbf{G}^{v\prime} = \begin{pmatrix} 0 \\ \tau'_{yx} \\ \tau'_{yy} \\ u'\tau'_{yx} + v'\tau'_{yy} + \kappa T'_y \end{pmatrix},$$

where t is physical time and x and y are the Cartesian coordinates. ρ denotes density, u and v

the x- and y-direction velocity components, E the specific total energy, T the temperature and κ the heat conduction coefficient calculated from the constant Prandtl number $\mathrm{Pr} = 1$. ρ_0, $(\rho E)_0$ and $(\rho H)_0$ denote the stagnation values of density, total energy density and total enthalpy density, respectively. The perturbation variables are given as follows

$\rho' = \rho - \rho_0, \quad (\rho\mathbf{u})' = (\rho\mathbf{u}), \quad (\rho E)' = \rho E - (\rho E)_0, \quad (\rho H)' = (\rho E)' + p'$

$\mathbf{u}' = \frac{(\rho\mathbf{u})'}{\rho_0+\rho'}, \quad \tau' = \mu(\nabla\mathbf{u}' + (\nabla\mathbf{u}')^T) - \frac{2}{3}\mu(\nabla\cdot\mathbf{u}')\mathbf{I}, \quad T' = \frac{p'/R - \rho' T_0}{\rho_0+\rho'}$

Here, R is the specific gas constant and μ is the viscosity which is determined from the Sutherland law $\frac{\mu}{\mu_0} = (\frac{T}{T_0})^{1.5}[(1+S_c)/(\frac{T}{T_0}+S_c)]$ with non-dimensional Sutherland constant $S_c = \frac{110}{301.75}$.

Since perfect gas is considered, the pressure perturbation can be related to the conservative perturbation variables $p' = (\gamma-1)[(\rho E)' - \frac{1}{2}((\rho\mathbf{u}'\cdot\mathbf{u}'))]$, where the ratio of specific heats $\gamma = c_p/c_v = 1.4$ for air.

The viscous flux vectors $\mathbf{F}^{v\prime}$ and $\mathbf{G}^{v\prime}$ are the same as for the standard conservative form, except for using the temperature perturbation T' instead of temperature T for the heat flux terms. The momentum density and velocity perturbations are taken as the same as their unperturbed counterparts, i.e. $(\rho\mathbf{u})' = \rho\mathbf{u}$ (Larsson and Müller, 2009). For convenience the variables are non-dimensionalized with ρ_0, stagnation speed of sound c_0, L the length of the flexible plate and $\rho_0 c_0^2$ as reference values. In order to generalize the geometry for the human upper airways, the equations of motions are transformed from the physical domain (x, y) to the computational domain (ξ, η) by the following relations, and obviously for time-dependent geometry the transformation depends on time as well.

$$\begin{aligned} t &= \tau \\ x &= x(\xi,\eta,\tau) \\ y &= y(\xi,\eta,\tau). \end{aligned} \tag{2}$$

Thus, the transformed 2D compressible Navier–Stokes equations in perturbation form are expressed as

$$\hat{\mathbf{U}}'_\tau + \hat{\mathbf{F}}'_\xi + \hat{\mathbf{G}}'_\eta = 0, \tag{3}$$

where $\hat{\mathbf{U}}' = J^{-1}\mathbf{U}'$, $\hat{\mathbf{F}}' = J^{-1}(\xi_\tau\mathbf{U}' + \xi_x(\mathbf{F}^{c\prime} - \mathbf{F}^{v\prime}) + \xi_y(\mathbf{G}^{c\prime} - \mathbf{G}^{v\prime}))$ and $\hat{\mathbf{G}}' = J^{-1}(\eta_\tau\mathbf{U}' + \eta_x(\mathbf{F}^{c\prime} - \mathbf{F}^{v\prime}) + \eta_y(\mathbf{G}^{c\prime} - \mathbf{G}^{v\prime}))$. The chain rule for partial differentiation provides the expressions for Cartesian derivatives in the viscous flux vectors $\mathbf{F}^{v\prime}$ and $\mathbf{G}^{v\prime}$, e.g. $u'_x = u'_\xi\xi_x + u'_\eta\eta_x$ and $u'_y = u'_\xi\xi_y + u'_\eta\eta_y$. The Jacobian determinant of the transformation is $J^{-1} = x_\xi y_\eta - x_\eta y_\xi$ and time-dependent metric terms are

$$\begin{aligned} J^{-1}\xi_x &= y_\eta, \quad J^{-1}\xi_y = -x_\eta, \quad J^{-1}\xi_\tau = -x_\tau\xi_x + y_\tau\xi_y, \\ J^{-1}\eta_x &= -y_\xi, \quad J^{-1}\eta_y = x_\xi, \quad J^{-1}\eta_\tau = -y_\tau x_\xi + x_\tau y_\xi. \end{aligned} \tag{4}$$

2.1.1. Numerical schemes

The high order finite difference method based on SBP operators (Strand, 1994; Gustafsson, 2008; Gustafsson et al., 1995) is employed for space discretization of the compressible Navier–Stokes equations. We use a globally fourth order SBP operator to discretize the first ξ- and η-derivatives in (4) and (3) and apply them twice to approximate the viscous parts of $\hat{\mathbf{F}_\xi}'$ and $\hat{\mathbf{G}_\eta}'$. The SBP operators for $\frac{\partial}{\partial\xi}$ and $\frac{\partial}{\partial\eta}$ correspond to the sixth order central difference operator in the interior but degrade to third order accuracy near the boundary, resulting in fourth order global accuracy (Gustafsson, 2008). This approach is based on the energy method, which permits us to derive well-posedness for the continuous problem and to guarantee stability for the discrete problem. The summation by parts operators and the stability criteria are discussed in detail in the Appendix.

For the time integration process, the classical fourth order explicit Runge–Kutta method is used. A time step size $\triangle t$ corresponding to CFL = 0.333 is chosen to ensure stability.

The multi-block structured grid approach is employed to represent the simplified geometry in the upper airways. Fig. 2(a) shows that we employ 6 blocks. Blocks 1, 3 and 5 have the lower channel wall as their southern boundaries and the rigid plate, flexible plate and the line between the trailing edge of the flexible plate and the outlet, respectively, as their northern boundaries, cf. lower plot in Fig. 2(a). The upper neighbouring blocks 2, 4 and 6 with the upper channel wall as their northern boundaries are set apart in the upper plot of Fig. 2(a) to show the overlapping regions. The decomposition of the computational domain into blocks allows us to accommodate geometric flexibility with high order operators. Having an overlap region of grid points at the block interfaces, a smooth transition of the numerical solution from one block to another block is achieved. For the seven-point stencil of the standard sixth order central finite difference method, a three-point overlap at each side of inter-block boundaries is added cf. Fig.2(b). The black points are located on the non–overlapping block boundary. The three red points in the interior of the left block communicate their data to the overlapping white points of the right block. Likewise, the three green points in the interior of the right block communicate their data to the overlapping white points of the left block. The inter-block communication between neighbouring blocks is accomplished by using the Message Passing Interface (MPI) such that each block is assigned to a single process, enabling parallel solution of the flow field.

This fluid solver has been validated in previous investigations (Müller, 2008; Larsson and Müller, 2012) for single-domain structured grids.

2.1.2. Boundary conditions

Adiabatic no-slip boundary conditions are applied on the walls and the fluid-structure interface. At the inflow, the velocities in the x- and y-directions are imposed using a uniform inlet profile normal to the boundary, $u(x = 0, t) = U_0$ and $v = 0$. In addition, the inlet temperature is set to $T = T_0 = 310$ K. The outlet pressure is set to atmospheric pressure, i.e., $p' = p - p_0 = p - p_{\text{atm}} = 0$ Pa. Non-reflecting characteristic boundary conditions are employed at the inflow and outflow boundaries to minimize wave reflections. The Navier–Stokes characteristic boundary conditions (NSCBC) developed by Poinsot and Lele (1992) are employed to approximate incoming waves based on local one-dimensional inviscid (LODI) relations. The primitive variables can be related to the wave amplitude ($\mathscr{L}_i$) by LODI relations. The amplitudes of the characteristic waves are $\mathscr{L}_1 = \lambda_1(\frac{\partial p}{\partial x} - \rho c\frac{\partial u}{\partial x})$, $\mathscr{L}_2 = \lambda_2(c^2\frac{\partial \rho}{\partial x} - \frac{\partial p}{\partial x})$, $\mathscr{L}_3 = \lambda_3(\frac{\partial v}{\partial x})$ and $\mathscr{L}_4 = \lambda_4(\frac{\partial p}{\partial x} + \rho c\frac{\partial u}{\partial x})$. Since fully non-reflecting conditions may lead to an ill-posed problem (Poinsot and Lele, 1992), this approach is partially reflecting. Imposing a constant pressure at the outlet requires $\mathscr{L}_1 = -\mathscr{L}_4$. To keep the reflections low and pressure close to atmospheric pressure, the incoming wave amplitude is set to

$$\mathscr{L}_1 = K(p - p_{atm}), \tag{5}$$

where K is the relaxation coefficient. Rudy and Strikwerda proposed the relaxation coefficient as $K = \sigma(1 - \text{Ma}^2)(c/L_t)$ where Ma is the Mach number, c the sound speed, L_t the total length of the domain and σ a constant value (Rudy and Strikwerda, 1980). The optimum value $\sigma = 0.25$ derived by Rudy and Strikwerda (1980) is employed. For reverse flow (negative velocity in x-direction) at the outlet, $\mathscr{L}_1$, $\mathscr{L}_2$ and $\mathscr{L}_3$ are set to zero.

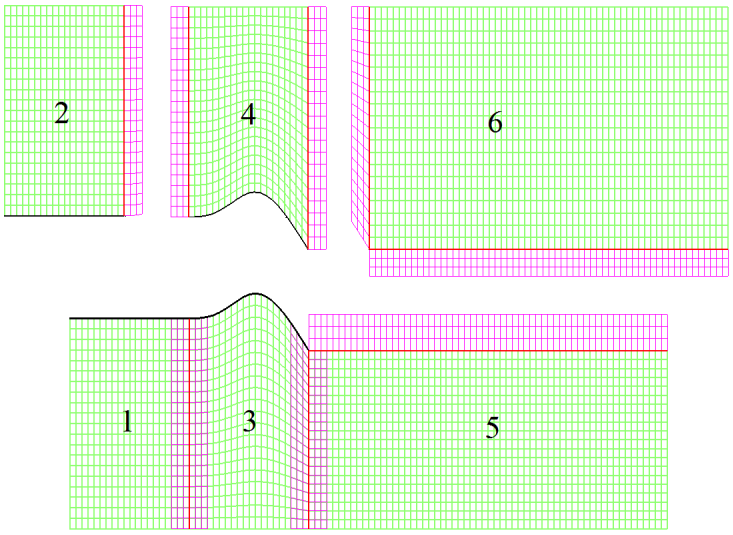

(a) Block-structure topology of the computational domain. The three upper blocks are detached in the figure for illustration of the three-point overlap, shown with magenta lines.

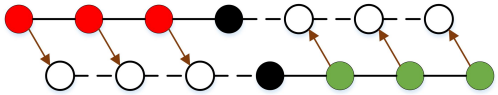

(b) Illustration of points overlapping along a line. The black points lie on the block boundary, the red and green points are internal points in different blocks, the white points are added ghost points which overlap the internal points in the other block, and the arrows indicate the direction of data transfer between blocks.

Figure 2: Multiblock topology used for the simplified geometry of the upper airways.

2.2. The structure model

In the present study, the motion of the thin plate is based on the linear Euler–Bernoulli thin beam theory. This theory provides the correlation between the deflection of the beam and the applied load. In the Euler–Bernoulli thin beam theory, the deflection is assumed to be unidirectional in the normal direction of the thin beam. Thus, deflection occurs only as a result of bending; the shear-deformation and normal strains are neglected. There is no contribution from the fluid shear stress, i.e., viscous effects on the plate are ignored and only the difference in fluid pressure is accounted for. The oscillation of the flexible plate is constrained to vertical direction without any stretch along the horizontal direction. The governing equation for the vertical displacement $\phi(x,t)$ is expressed as

$$\rho_s h \frac{\partial^2 \phi}{\partial t^2} + d\frac{\partial \phi}{\partial t} + B\frac{\partial^4 \phi}{\partial x^4} = -\delta p, \tag{6}$$

where ρ_s, h, d and B denote respectively the density, thickness, flexural rigidity and structural damping of the plate, and δp denotes the applied pressure load. The flexural rigidity B is defined by $B = Eh^3/[12(1-\nu^2)]$, where E and ν are the elastic modulus and Poisson ratio, respectively. The

variables in Eq. (6) are non-dimensionalized with respect to the stagnation density ρ_0, stagnation speed of sound c_0 and the length of the flexible plate L, in the same way as for the fluid solver.

The equation for calculating the energy of the plate per unit width can be derived by multiplying Eq. (6) by $\dot{\phi} = \frac{\partial \phi}{\partial t}$ and integrating over the length of the plate L (Balint and Lucey, 2005).

$$\frac{d}{dt}\left(\overbrace{\underbrace{\frac{1}{2}\rho_s h \int_0^L \dot{\phi}^2 dx}_{E_k} + \underbrace{\frac{1}{2}B\int_0^L (\phi_{xx})^2 dx}_{E_s}}^{E_t}\right) = \underbrace{\int_0^L (-\delta p)\dot{\phi} dx}_{\dot{W}} - \underbrace{d\int_0^L \dot{\phi}^2 dx}_{\dot{D}_\phi}. \tag{7}$$

The left hand side of the Eq. (7) is the time derivative of the total energy of the plate E_t composed of the kinetic and strain energies, E_k and E_s, respectively. The right hand side represents the rate of work done by the fluid on the plate $\dot{W}$ and the rate of energy dissipation due to damping of the plate $\dot{D}_\phi$.

2.2.1. Computational methods

The Newmark time integration method (Newmark, 1959) is employed for solving Eq.(6) implicitly. The displacement and velocity from time step t are integrated to $t + \triangle t$ using the relations

$$\dot{\phi}^{n+1} = \dot{\phi}^n + [(1-\gamma)\ \ddot{\phi}^n + \gamma \ddot{\phi}^{n+1}]\triangle t, \tag{8}$$

$$\phi^{n+1} = \phi^n + \dot{\phi}^n \triangle t + [(\frac{1}{2} - \beta)\ddot{\phi}^n + \beta \ddot{\phi}^{n+1}]\triangle t^2, \tag{9}$$

where γ and β are parameters of the Newmark scheme and $\ddot{\phi}^{n+1}$ is the acceleration at the new time level.

The most accurate, unconditionally stable scheme of the Newmark family is used. Its coefficients are $\beta = 1/4$ and $\gamma = 1/2$. The scheme is second order accurate and preserves the energy for the linear system (Hughes, 2012). The standard second order central difference discretization is used for the fourth order spatial derivative $(\phi_{xxxx})_j^{n+1} \approx \frac{1}{\triangle x^4}(\phi_{j+2}^{n+1} - 4\phi_{j+1}^{n+1} + 6\phi_j^{n+1} - 4\phi_{j-1}^{n+1} + \phi_{j-2}^{n+1})$. The integration scheme works by first computing the updated displacement and applying it to obtain the structure acceleration at the new time level, and then finding the updated velocity of the structure.

2.2.2. Boundary conditions

The cantilevered flexible plate is clamped at the leading edge and free at the trailing edge. For a clamped configuration the first two nodes are stationary. The continuous and discrete boundary conditions read

$$\begin{array}{ll} \phi(0,t) = 0, & \phi_1 = 0, \\ \frac{\partial \phi(0,t)}{\partial x} = 0, & \phi_1 = \phi_2. \end{array} \tag{10}$$

For a free end configuration it is assumed that the bending moment and shear force are zero at the last node. Thus, we have

$$\begin{array}{ll} \frac{\partial^2 \phi(L,t)}{\partial x^2} = 0, & \phi_{N-1} = 2\phi_{N-2} - \phi_{N-3}, \\ \frac{\partial^3 \phi(L,t)}{\partial x^3} = 0, & \phi_N = 3\phi_{N-2} - 2\phi_{N-3}. \end{array} \tag{11}$$

2.3. Fluid-structure interaction

The Arbitrary Lagrangian–Eulerian (ALE) formulation is employed to handle the fluid flow in Eulerian description using moving fluid grids and the plate structure in a Lagrangian formulation using stationary structure grids. In the time-dependent coordinate transformation of the fluid flow domain, the grid point velocities $\dot{x}$ and $\dot{y}$ are subtracted from the fluid velocity to define the contravariant velocity components $U = \xi_x(u - \dot{x}) + \xi_y(v - \dot{y})$ and $V = \eta_x(u - \dot{x}) + \eta_y(v - \dot{y})$ which yield simple expressions for the transformed inviscid flux vectors $\hat{\mathbf{F}}^c$ and $\hat{\mathbf{G}}^c$ (Pulliam and Steger, 1980). The mesh update is implemented by remeshing the whole fluid domain in each time step using the positions and velocities of the flexible structure at the boundary and a linear interpolation for interior points in the fluid domain.

Solving fluid flow on a moving mesh, the numerical scheme should satisfy the Geometric Conservation Law (GCL) for mathematical consistency (Visbal and Gaitonde, 2002). This law states that

$$(J^{-1})_\tau + (J^{-1}\xi_t)_\xi + (J^{-1}\eta_t)_\eta = 0, \tag{12}$$

where the time derivatives of the computational coordinates ξ and η are calculated from grid point velocities $\dot{x} = x_\tau,\ \dot{y} = y_\tau$ as follows

$$\xi_t = -\xi_x\dot{x} - \xi_y\dot{y}, \quad \eta_t = -\eta_x\dot{x} - \eta_y\dot{y}. \tag{13}$$

Then, the 2D Navier–Stokes equations in ALE formulation (Peyret et al., 1975) are given by

$$\mathbf{U}'_\tau = \tfrac{1}{J^{-1}}(-\hat{\mathbf{F}}'_\xi - \hat{\mathbf{G}}'_\eta - (J^{-1})_\tau\mathbf{U}'), \tag{14}$$

where $\hat{\mathbf{F}}' = J^{-1}(\xi_t\mathbf{U}' + \xi_x\mathbf{F}' + \xi_y\mathbf{G}')$ and $\hat{\mathbf{G}}' = J^{-1}(\eta_t\mathbf{U}' + \eta_x\mathbf{F}' + \eta_y\mathbf{G}')$ are the transformed flux vectors.

The coupling between the fluid and the structure is handled by an explicit, two-way method where forces and deformations are exchanged between the flow and the deformable structure in each time-step, as shown in Figure 3. The fluid and structure interact with each other by applying equal vertical displacement and velocity at the interface, satisfying the no-slip and adiabatic wall boundary conditions.

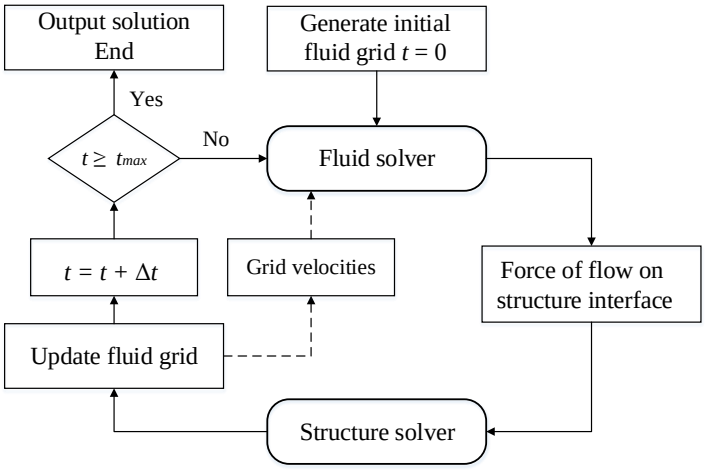

Figure 3: Schematic of two way coupling model.

3. Results and discussion

3.1. Verification of structure solver in vacuum

3.1.1. Eigenmode analysis

The numerical schemes for the structural model have been verified through the plate oscillation in vacuum associated with its eigenmodes. Following the work by Balint and Lucey (2005), d and δp in Eq. (6) are set to zero. Assuming a harmonic vibration of time dependency $e^{i\omega t}$, Eq. (6) can be rewritten based on the harmonic vibration. Thus, for vibration in vacuum, the cantilevered plate has the eigenfunctions

$$\begin{aligned}&\phi_m(x) = A\,[(\cosh(k_m x) - \cos(k_m x)) - \tfrac{\cosh(k_m L)+\cos(k_m L)}{\sinh(k_m L)+\sin(k_m L)}\,(\sinh(k_m x) - \sin(k_m x))],\\ &m = 1, 2, 3, \ldots \infty\end{aligned} \tag{15}$$

where A denotes the amplitude scaling constant and $k_m = \beta_m/L$ the characteristic wavenumber obtained by finding the roots of an eigenvalue equation. The coefficients β_m are obtained from

$$\cosh\beta_m \cos\beta_m + 1 = 0. \tag{16}$$

The five first values of β_m, $m = 1, ..., 5$, are $1.875, 4.694, 7.855, 10.996, 14.137$. The angular eigenfrequencies can be calculated as

$$\omega_m = k_m^2\sqrt{B/(\rho_s h)}. \tag{17}$$

The modal configurations of the cantilevered plate are shown in Figure 4.

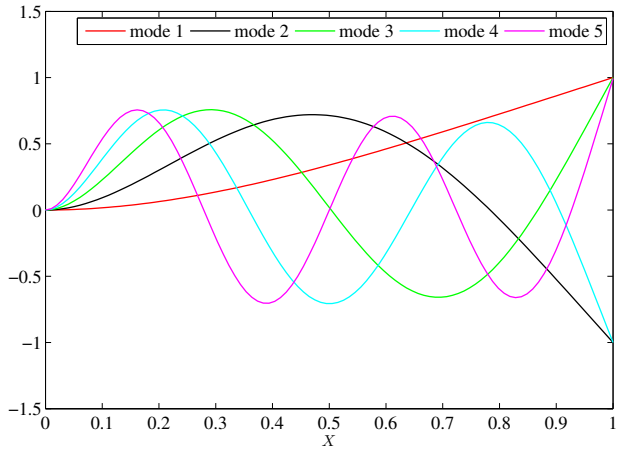

Figure 4: The first five eigenfunctions $\phi_m(x)$ with $A = 1$ in Eq.(15).

3.1.2. Comparison with analytical solution

Our numerical schemes have been first verified and tested by simulating plate oscillation in vacuum associated with the second eigenmode of the structure. The physical properties of the flexible structure were taken the same as in the study by Balint and Lucey (2005), namely $m = 2.6$ kg/m^2, $B = 4.92$ kN m and the length of the flexible structure $L = 2$ m. The number of grid points for discretizing the plate was set to $N = 201$ and the time step size was set to $\Delta t = 5 \times 10^{-6}$ s. The plate was initially deformed using the amplitude $A = 0.01$ m in Eq. (15). Figure 5 illustrates

the time variation of the plate deformation, the displacement of the tip position and the oscillating frequency. The frequency is calculated by performing a fast Fourier transform (FFT) on the time history of the tip displacement of the plate. The error between the analytical solution of the second mode eigenfrequency $\omega_2 = 38.1366$ Hz in Eq. (17) and the computed frequency $\omega_2 = 38.0906$ Hz amounts to 0.12 %.

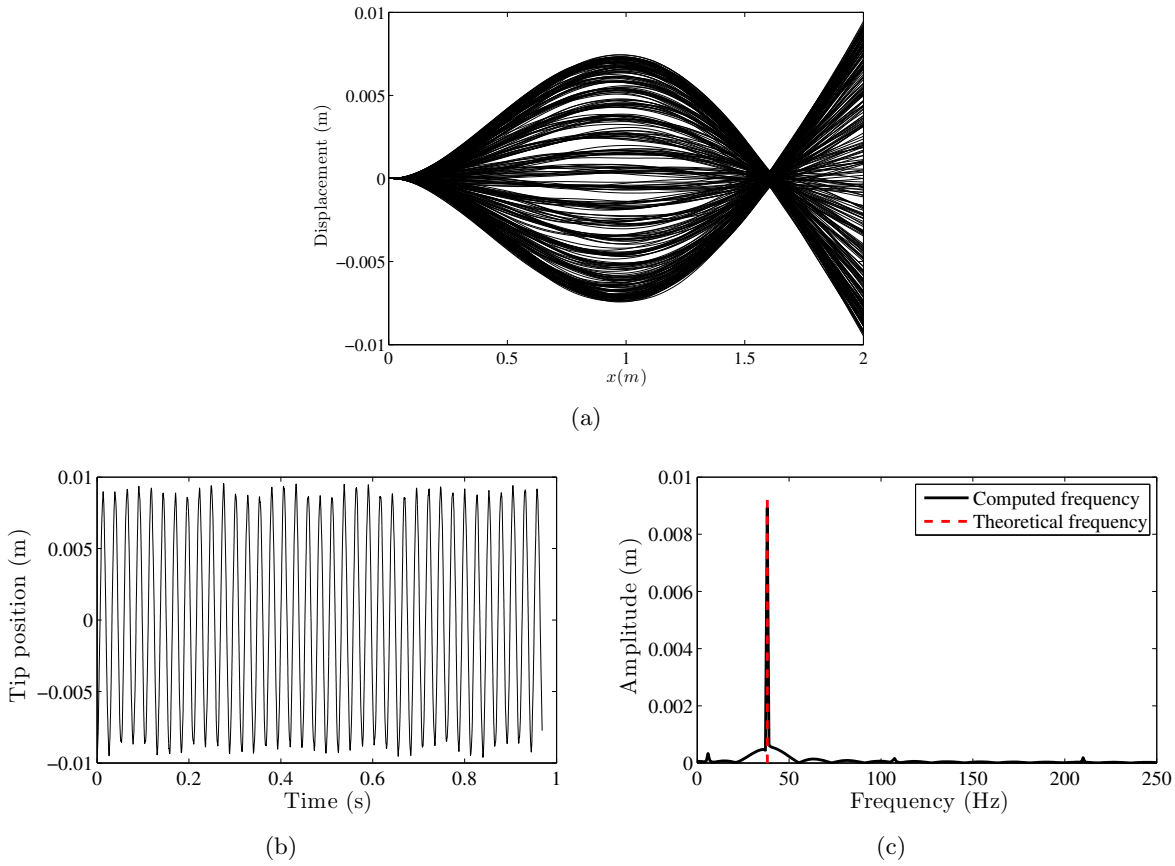

Figure 5: (a) Sequence of flexible plate deformation in the second eigenmode, (b) time history of the displacement of the trailing edge (tip), (c) oscillation frequency of displacement of trailing edge (tip).

3.2. Problem description and initial conditions for fluid–structure interaction

The problem domain consists of a horizontal channel with an interior wall representing the hard and soft palate along the center-line (cf. Fig. 1), dividing the inlet boundary into an upper and a lower inlet. We allow the inlet boundary to operate in two different configurations: one where both inlets have uniform inflow of air, and one where only the upper inlet has inflow while keeping the lower inlet at zero velocity. The flexible plate has length $L = 8$ mm, and the streamwise length and duct height (H) are 40 mm and 9.6 mm, respectively, cf. Fig.1(a).

The flexible plate is initially displaced using an eigenfunction. To initialize the flow field, we keep the flexible plate fixed in its initial position and integrate the flow solver in time from stagnant flow $\mathbf{U}' = 0$, except for the inlet velocity, until an approximately steady state flow solution has been reached. Thereafter, the flexible plate is released from its initial position and allowed to interact

with the flow.

As mentioned above, for a linear cantilevered plate with length L and flexural rigidity B, the vertical displacement $\phi_m(x)$ of the m^{th} eigenmode can be described by Eq. (15). In the present study, only the second eigenmode is considered for the initial plate displacement, mainly due to the fact that this mode has been known to be responsible for the soft palate flutter (Huang, 1995).

3.3. Verification of fluid–structure interaction

To assess the validity of the present solver, grid independence was investigated by computing the oscillation frequency of the flexible plate on coarse and fine grids. The fluid density was set to $\rho = 1.18$ kg/m^3 based on $T = 301.75$ K. We used the Reynolds number $\text{Re} = \frac{\rho U L}{\mu} = 378$ and the Mach number $\text{Ma} = \frac{U}{c_0} = 0.01$ based on inlet velocity ($U = 0.32$ m/s), speed of sound and length of the plate. The speed of sound was deliberately reduced to speed up the computation. The dynamic viscosity and other fluid properties were calculated as discussed in section 2.1. The initial tip amplitude was given by $\phi(L, 0)/H = 0.2$. The elastic modulus and Poisson ratio were $E = 880$ MPa and $\nu = 0.3333$, respectively, with a plate density of $\rho_s = 2477$ kg/m^3, plate thickness of $h = 10^{-5}$ m and an undamped thin plate, i.e., $d = 0$ N s/m^3. Therefore, the plate is modeled as an infinitely thin 1D plate with the thickness parameter h chosen to obtain the desired second mode eigenfrequency. Using these values, the analytical second mode frequency in vacuum determined by Eq. (17) is 100 Hz. Numerically, the second in vacuum eigenfrequency is computed with $N = 101$ grid points and $\Delta t c_0/L = 0.001$ as 99.18 Hz which agrees well with the analytical value with a 0.82% error.

Fig. 6 shows the time history of the tip displacement from coarse to fine grids. Since the solution on the last two fine grids agree quite well, the 501×201 grid is adopted as a sufficiently fine grid. The oscillation frequency and the time variation of the plate deformation for fine grid are shown in Fig. 7. The oscillation frequency of the flexible plate for the fine grid is obtained at 91.5 Hz (corresponding to the non-dimensional frequencies, $f^*_{c_0} = f\frac{L}{c_0} = 0.022875$ based on speed of sound c_0 and $f^*_U = f\frac{L}{U} = 2.2875$ based on inlet velocity U). Note that the in vacuum second mode frequency for the undamped flexible plate has been obtained by setting the external force (pressure difference) to zero in Eq. (6). However, in the simulation of fluid–structure interaction the pressure difference provides the external force which drives the plate oscillation. According to the measurements performed by Brietzke and Mair (2006), the palatal oscillation frequency of snoring ranges from 21 to 323 Hz with an average of 89.4 Hz.

In the following, the temporal discretization error of the fluid–structure interaction is investigated for the tip displacement of the plate. The parameters are identical to those used for the 501×201 fine grid in section 3.3 while varying the time step sizes. The tip displacement of the flexible plate is plotted versus time for five cycles of oscillation in Fig. 8. The time step sizes Δt are varied such that the CFL numbers become CFL ≈ 1/3, 1/6, 1/12 and 1/24. Fig. 8 shows that the time history of the tip displacment is hardly affected by the time step size.

3.4. Simulation of plate oscillation

3.4.1. Both inlets open

The time sequence of vorticity contours for the case when both inlets are open is shown in Fig. 9. The initial tip displacement is $\phi(L, 0)/H = 0.2$, $\text{Re} = 378$ and $\text{Ma} = 0.01$. At time $tc_0/L = 0$ (when the flexible plate is released from its initial displacement after steady state has been reached), boundary layers have been established at the channel walls, rigid and flexible structures and the

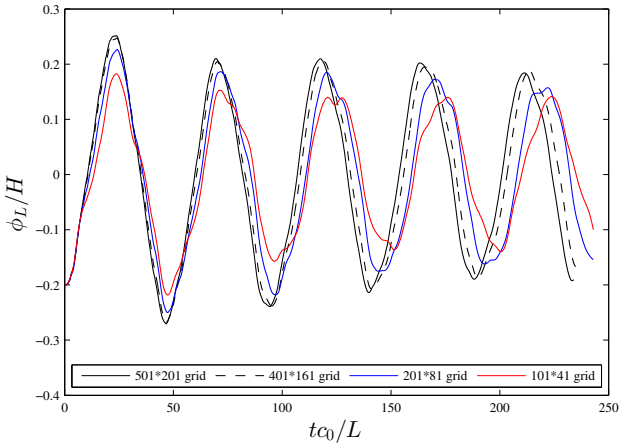

Figure 6: Test of grid independence, time history of tip displacement.

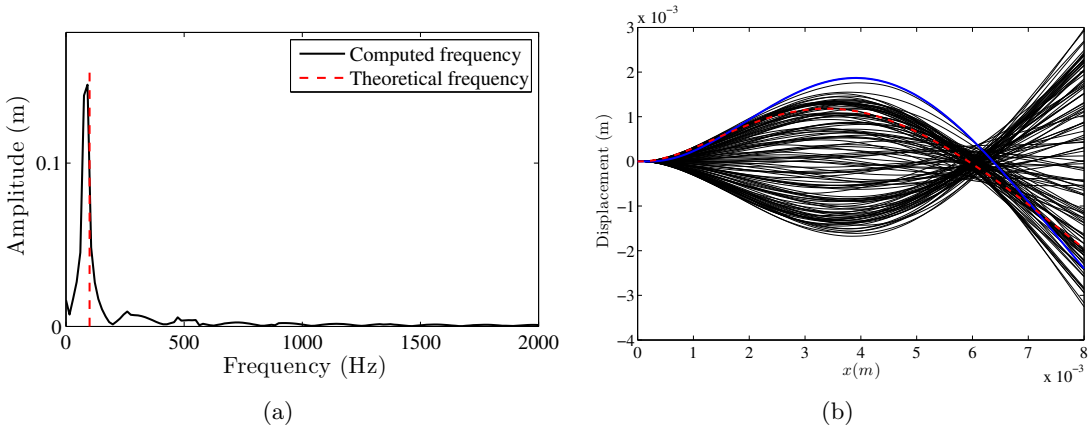

Figure 7: (a) Oscillation frequency of displacement of trailing edge (tip) for the fine grid, (b) sequence of flexible plate deformation for five cycle oscillations, the initial and final deformation are marked by solid blue line and red dashed lines, respectively.

flow is already separated from the trailing edge. At $tc_0/L = 8$ corresponding to $tU/L = 0.08$, the third vortex leaving the trailing edge is observed. The first and second vortices are about to pair and create a strong vortex at $tc_0/L = 13$. The fourth vortex is about to separate from the tip of the plate at $tc_0/L = 25$. The leading vortex rolls up at $tc_0/L = 39$. The vortex shedding from the trailing edge repeats itself almost symmetrically. The vortices formed as a result of the oscillation of the flexible plate and the interaction with the fluid flow are convected downstream. During the processes, the interaction between the vortices sometimes leads to vortex pairing.

To ensure that the outlet boundary conditions in this channel do not affect the vortices, this simulation is repeated for a longer channel. Fig. 10 shows the results. The only difference between Fig. 10 and Fig. 9 is that the length of the outlet blocks (from trailing edge of the plate towards outlet boundary in Fig. 1) and the number of grid points in these blocks have been doubled ($6L$

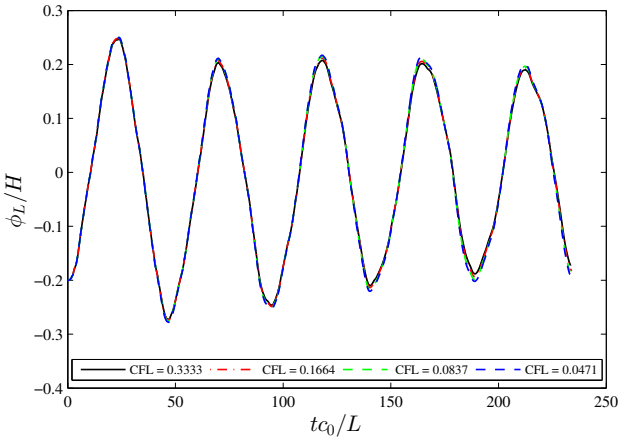

Figure 8: Test of time step independence, time history of tip displacement for five cycles of oscillation.

instead of $3L$ in Fig.1). The first and second snapshots show the status of the vortices at the same time for these two different channels. Except for the vortex close to the outlet being a little smaller and a little closer to centerline in the simulation with the longer channel at the considered time instant, the results for the two different channel lengths are in excellent agreement.

3.4.2. Lower inlet closed

Fig. 11 represents the results of vorticity contours when the lower inlet is closed. The initial tip amplitude is $\phi(L,0)/H = 0.1$, Reynolds number and Mach number based on inlet velocity U=0.64 m/s are equal to 756 and 0.02, respectively. The leading vortices are already shed before the structure was released. At $tc_0/L = 9$, the leading vortex rolls up. The vortices near the trailing edge roll down at $tc_0/L = 27$. At $tc_0/L = 48$, the leading vortex is becoming weakened and pairing of the vortices near the trailing edge is observed. The vortex shedding tends to propagate towards the lower part of the domain, since the lower inlet is closed. Clearly, the vortex shedding is unsymmetrical. Vortex pairing occurring quite often creates a complex vortical structure.

3.5. The effect of plate properties

Since one of the surgical treatments of OSAS and snoring involves soft palate implants, the flow induced oscillation of the flexible plate with different material parameters is studied in this section. The structural model is governed by three parameters: mass, damping and stiffness. We used these parameters as control parameters to investigate the oscillation behaviour of the flexible structure in the fluid flow. The non-dimensional mass, rigidity and damping are defined as

$$m^* = \frac{\rho_s h}{L\rho_0}, \quad B^* = \frac{B}{L^3\rho_0 c_0^2}, \quad d^* = \frac{d}{\rho_0 c_0}. \tag{18}$$

Dividing these non–dimensional rigidity and damping of the plate by Ma^2 and Ma, respectively, gives us the non–dimensional quantities for B and d in incompressible flow using U^2 instead of c_0^2 and U instead of c_0, respectively. In order to examine the oscillation behaviour of the flexible structure, the Reynolds number and Mach number are fixed at 378 and 0.01, respectively. Figures

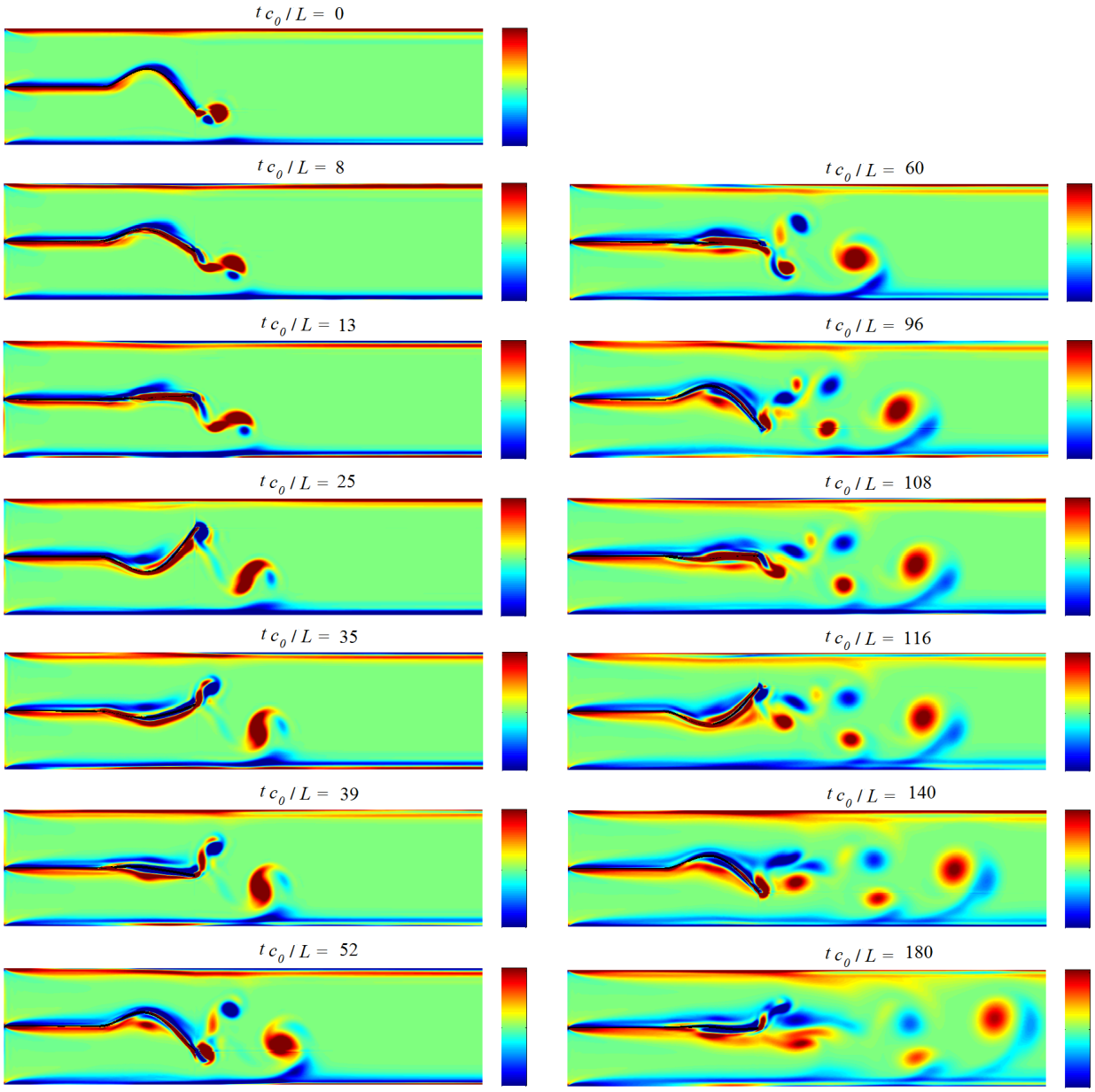

Figure 9: Time sequence showing vorticity contour plots, both inlets are open at Re = 378 and Ma = 0.01. The contour levels are from $-0.2\ \mathrm{s}^{-1}$ to $0.2\ \mathrm{s}^{-1}$ corresponding to $-5\times10^{-5} \leqslant (\bigtriangledown \times \mathbf{U})_z L/c_0 \leqslant 5\times10^{-5}$ and $-5\times10^{-3} \leqslant (\bigtriangledown \times \mathbf{U})_z L/U \leqslant 5\times10^{-3}$.

290 12, 14 and 16 illustrate the effect of changing the parameters on the displacement of the trailing edge.

The range of values of the non-dimensional mass is $m^* = 1.31 - 5.24$, as shown in Fig 12. The largest mass ratio decreases the oscillation frequency of the flexible plate to 61.06 Hz (non–dimensional frequency based on speed of sound $f^*_{c_0} = f\frac{L}{c_0} = 0.015265$ and based on inlet velocity

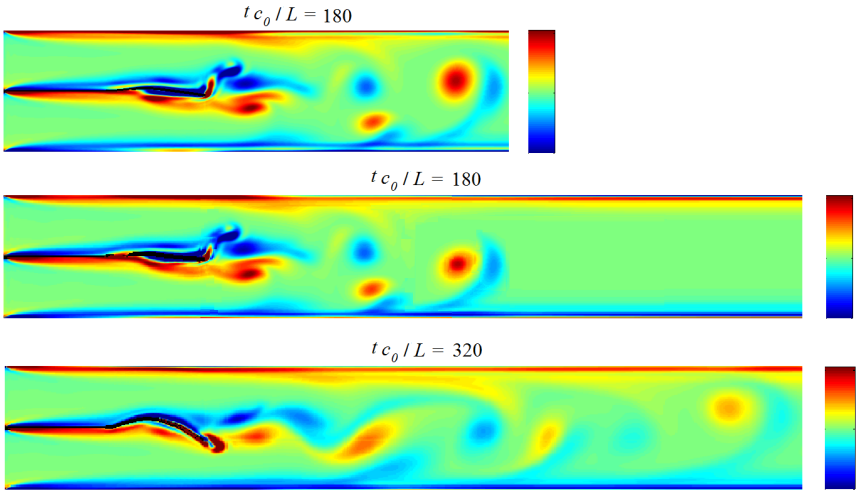

Figure 10: Time sequence showing vorticity contour plots, both inlets are open at Re = 378 and Ma = 0.01. The outlet blocks of two lower plots have a length of $6L$ instead of $3L$, cf. in Fig. 1, of the upper plot. The contour levels are from -0.2 s^{-1} to 0.2 s^{-1} corresponding to $-5 \times 10^{-5} \leqslant (\bigtriangledown \times \mathbf{U})_z L/c_0 \leqslant 5 \times 10^{-5}$ and $-5 \times 10^{-3} \leqslant (\bigtriangledown \times \mathbf{U})_z L/U \leqslant 5 \times 10^{-3}$.

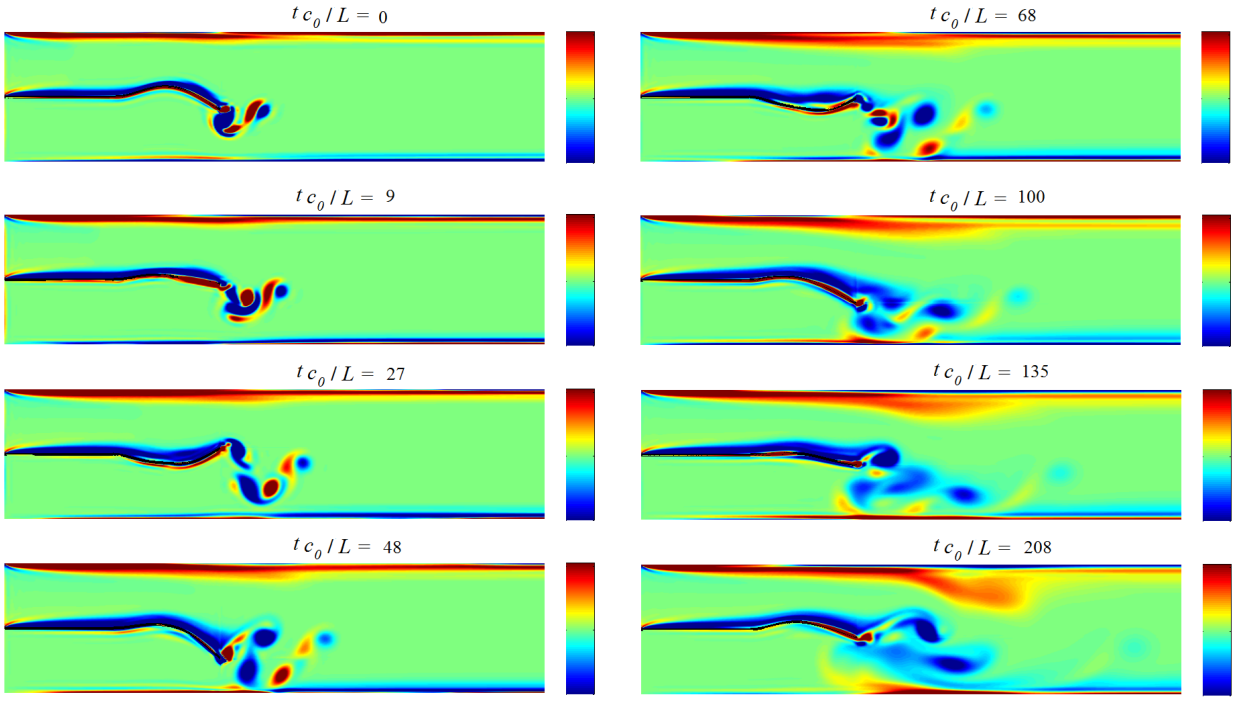

Figure 11: Time sequence showing vorticity contour plots, lower inlet is closed at Re = 756 and Ma = 0.02. The contour levels are from -0.2 s^{-1} to 0.2 s^{-1} corresponding to $-5 \times 10^{-5} \leqslant (\bigtriangledown \times \mathbf{U})_z L/c_0 \leqslant 5 \times 10^{-5}$ and $-5 \times 10^{-3} \leqslant (\bigtriangledown \times \mathbf{U})_z L/U \leqslant 5 \times 10^{-3}$.

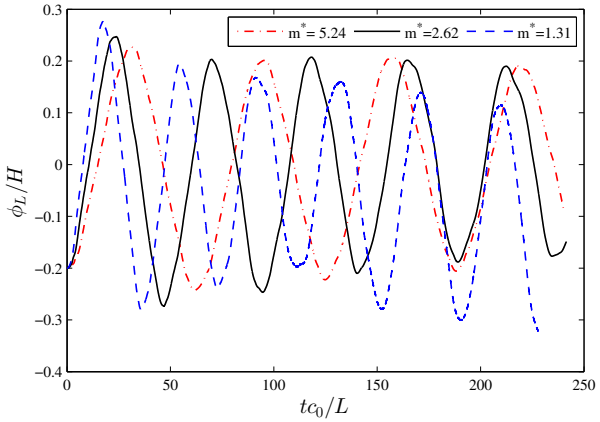

Figure 12: Time history of the tip displacement with different non-dimensional masses for undamped flexible plate (d^*=0) and fixed rigidity ($B^* = 1.3 \times 10^{-4}$).

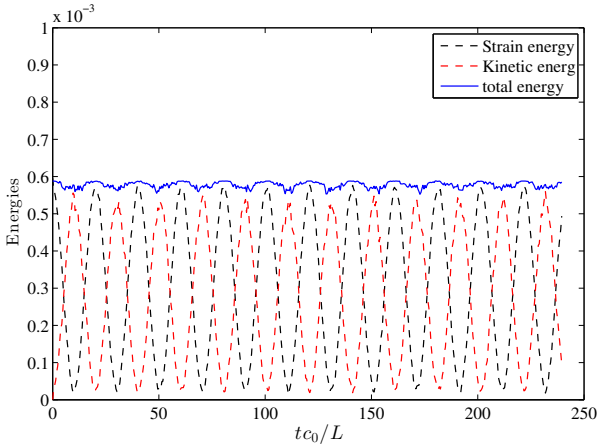

Figure 13: Evaluation of total energy E_t^*, strain energy E_s^* and kinetic energy E_k^* of the plate in vacuum for $m^* = 2.62$, $B^* = 1.3 \times 10^{-4}$ and $d^* = 0$.

$f_U^* = f\frac{L}{U} = 1.5265$) compared to the smallest one which enhances the oscillation frequency to 106.8 Hz ($f_{c_0}^* = 0.0267$ and $f_U^* = 267$). Figure 13 shows the total energy E_t^*, strain energy E_s^* and kinetic energy E_k^* of the plate in vacuum when the plate properties are $m^* = 2.62$, $B^* = 1.3 \times 10^{-4}$ and $d^* = 0$. It indicates that in the in vacuum situation the total energy of the plate remains nearly constant. Figure 14 gives the oscillation behaviour of the trailing edge as a representative of the flexible plate motion for three different non-dimensional rigidities. It is observed that for the higher rigidity case ($B^* = 2.6 \times 10^{-4}$) in the absence of damping, the oscillation frequency is higher, i.e. $f = 122$ Hz ($f_{c_0}^* = 0.0305$ and $f_U^* = 3.05$) than for $B^* = 1.3 \times 10^{-4}$ and $B^* = 6.6 \times 10^{-5}$ when $f = 91.5$ Hz ($f_{c_0}^* = 0.022875$ and $f_U^* = 2.2875$) and $f = 64$ Hz ($f_{c_0}^* = 0.016$ and $f_U^* = 1.6$), respectively. The non-dimensional total energies ($E_t^*(t) = E_s^*(t) + E_k^*(t)$) for these three different rigidities are illustrated in Fig. 15 showing oscillatory decrease (stable oscillation) of total energy for these cases. Furthermore, the transfer of energy between fluid flow and plate leads to larger amplitudes in the oscillation of the total energy compared to Fig. 13. Here, a warning is in place for the simulation with the largest stiffness $B^* = 2.6 \times 10^{-4}$. Our standard approach led to increasing total energy for $B^* = 2.6 \times 10^{-4}$, $d^* = 0$ and $m^* = 2.62$. Close inspection showed that the displacement of the structure developed high wavenumber oscillations. Solving the Euler–Bernoulli beam equation not as usual at every fluid time step, but at every other fluid time step led to a larger structure time step size, i.e., $\Delta t_s = 2\Delta t_f$. Choosing the time step size for the structure computation twice as large as the time step size for the flow computation, has a stabilizing effect and suppresses the numerical instability. Fig. 16 shows that in the presence of damping, the plate is gradually losing its oscillatory behaviour and reaches an undeformed shape. Fig. 17 compares the non-dimensional rate of work done by the fluid on the plate without damping and with two different damping coefficients. As expected, the damping coefficient has a large effect on whether the oscillations are damped or not.

3.6. Acoustic analysis

In this section, the acoustic pressure signal is analyzed to study the effect of plate oscillation on generating sound. Figs. 18 (a) and (c) demonstrate the time history of the acoustic pressure

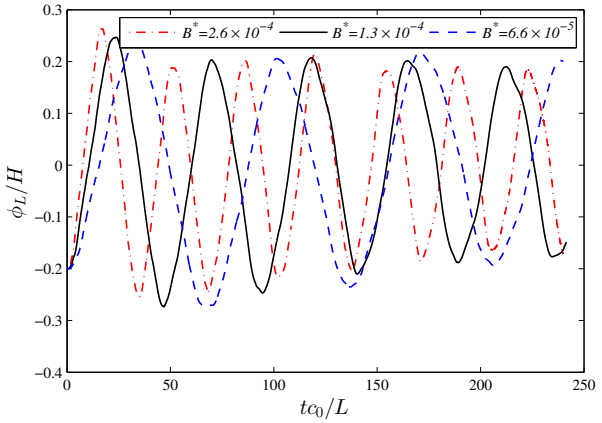

Figure 14: Time history of the tip displacement with different non-dimensional rigidities for undamped flexible plate (d^*=0) and fixed mass ($m^* = 2.62$). Note $\Delta t_s = 2\Delta t_f$ was used for $B^* = 2.6 \times 10^{-4}$.

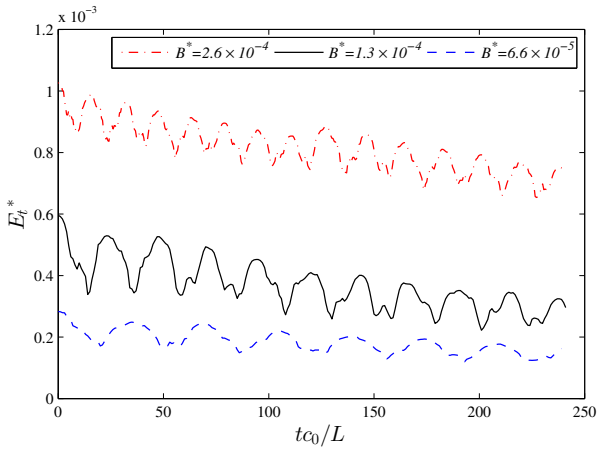

Figure 15: Evaluation of plate's total energy E_t^* for three different rigidities ($d^* = 0$, $m^* = 2.62$). Note $\Delta t_s = 2\Delta t_f$ was used for $B^* = 2.6 \times 10^{-4}$.

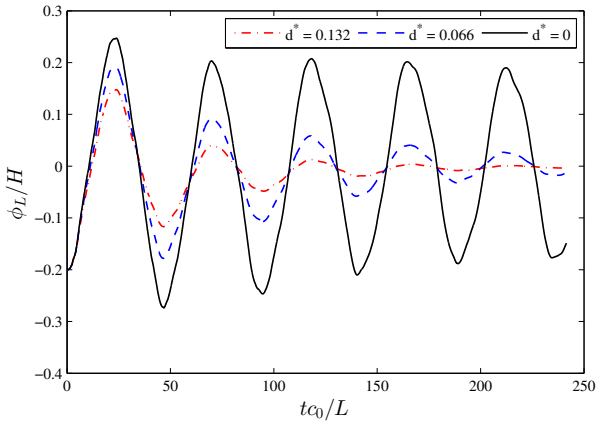

Figure 16: Time history of the tip displacement with different non-dimensional dampings and fixed mass and rigidity ($m^* = 2.62$, $B^* = 1.3 \times 10^{-4}$).

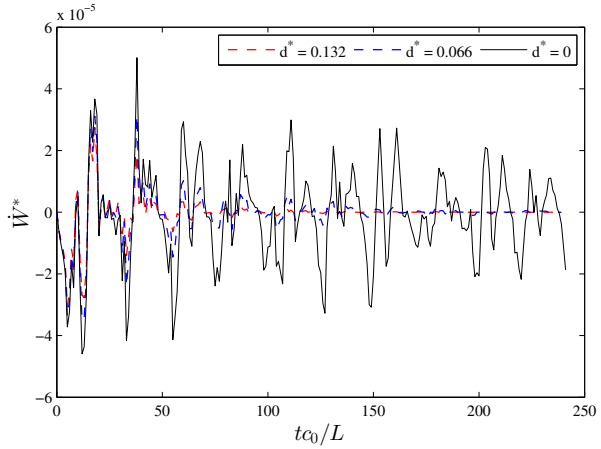

Figure 17: Variation of the non-dimensional rate of work done by the fluid on the plate ($m^* = 2.62$, $B^* = 1.3 \times 10^{-4}$).

for the simulation between $tc_0/L = 0$ and $tc_0/L = 240$. The flexible plate has its second mode initial configuration with $\phi(L,0)/H = 0.1$ as initial tip displacement. The Reynolds number and Mach number are 378 and 0.01, respectively. The initial flow field for this study was determined by simulating the flow field from $\mathbf{U}' = \mathbf{0}$, except for the inlet velocity, with the flexible plate fixed at its second mode position with $\phi(L,0)/H = 0.1$. The simulation was run until $tc_0/L = 40$, when steady state was approximately reached. The approximate solution was used as the initial condition for the present FSI for which the initial time was set as $tc_0/L = 0$. The acoustic pressure is recorded at four points, two points at $y = H/4$ and $y = 3H/4$ both near the inlet $x = L_t/10$ and near the outlet $x = 9L_t/10$, where L_t is the total length of duct and H the height of the

duct. The acoustic pressure is transformed to a spectrum by applying the fast Fourier transform (FFT), as shown in Figs. 18 (b) and (d). In the Fourier transform of the pressure signal, the frequencies as a consequence of the plate oscillation and the eigenfrequencies of the duct can be clearly distinguished.

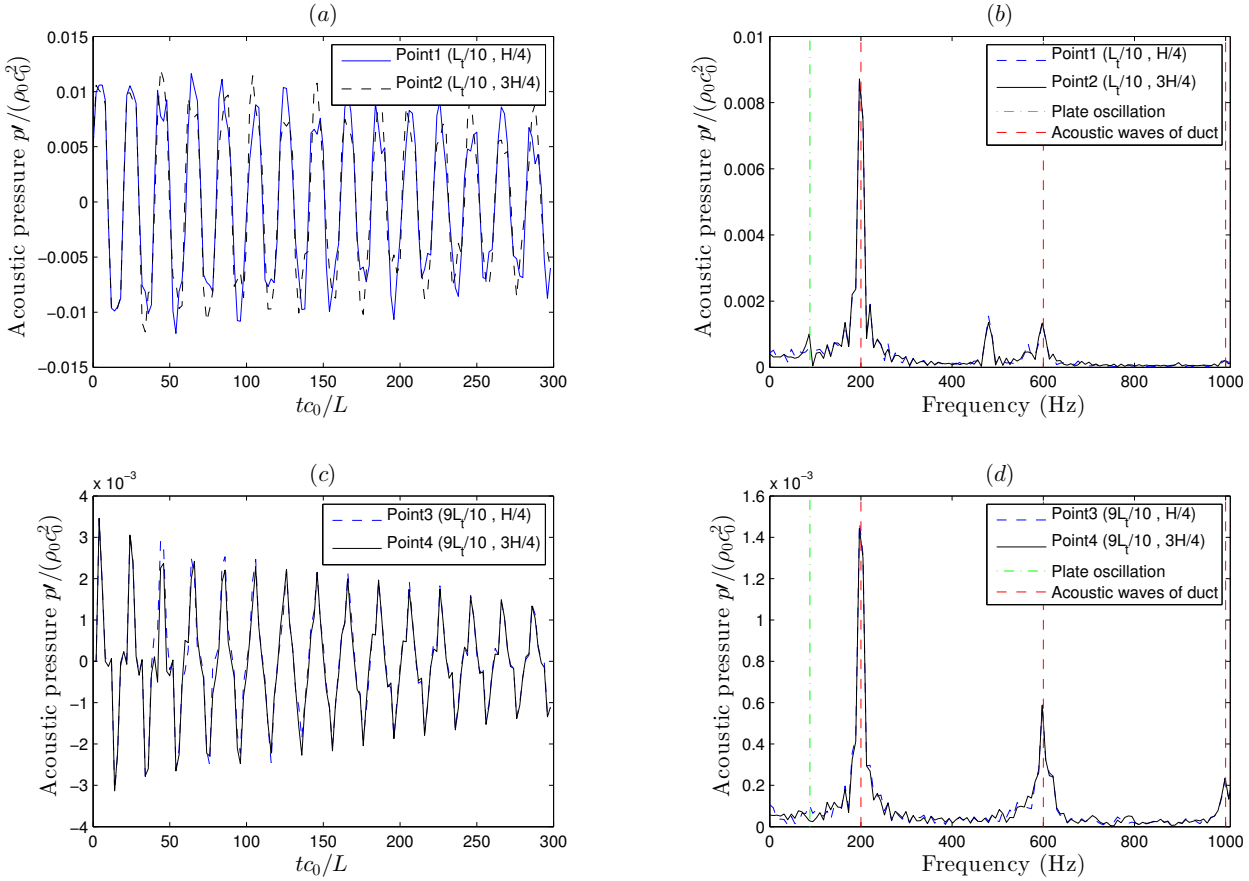

Figure 18: (a) and (c) Time history of acoustic pressure $p'/(\rho_0 c_0^2)$ at inlet and outlet, respectively; (b) and (d) Spectrum of pressure signal. The fluid flow is at Re = 378 and Ma = 0.01, the structure data are as in section 3.4, except for the initial tip displacement $\phi(L,0)/H = 0.1$. The flexible plate was released at $tc_0/L = 40$ corresponding to $tc_0/L = 0$ in plots (a) and (c).

The eigenfrequencies for an acoustically closed end duct with imposed velocity at inlet and outlet pressure (Selle et al., 2004) can be obtained as

$$f_n = (2n+1)(c/(4L_t)) \tag{19}$$

These represent the odd modes in terms of $n = 0, 1, ...$, where c is the speed of sound and L_t the total length of the duct (Selle et al., 2004). The first three modes predicted by Eq. (19) are observed in Fig. 18(b) and (d). It shows that the three first acoustic resonance frequencies of the duct appear in the spectrum of the computed pressure both near the inlet (Fig. 18(b)) and even clearer near the outlet (Fig. 18(d)).

We investigated means to reduce the reflections of the acoustic waves in the domain by means of non-reflecting boundary conditions with a simple scaling (Selle et al., 2004) and non-reflecting

boundary condition with plane wave masking (Polifke et al., 2006). However, the results using those approaches are not presented, because they were similar to the results obtained by the conditions explained in subsection 2.1.2. This similarity of the results obtained with the boundary conditions outlined in subsection 2.1.2 and with those by Selle et al. (2004) and Polifke et al. (2006) is not surprising, because those are also based on NSCBC by Poinsot and Lele (1992) like ours.

The spectrum analysis in Fig. 18(b) and (d) shows that the 1/4 wave mode (cf. Eq. (20)) pointed out by Selle et al. (2004) as the quarter wave mode frequency is dominant compared to the other harmonics and the frequency of plate oscillation.

$$f_0 = (1 - M^2)(c/(4L_t)) \tag{20}$$

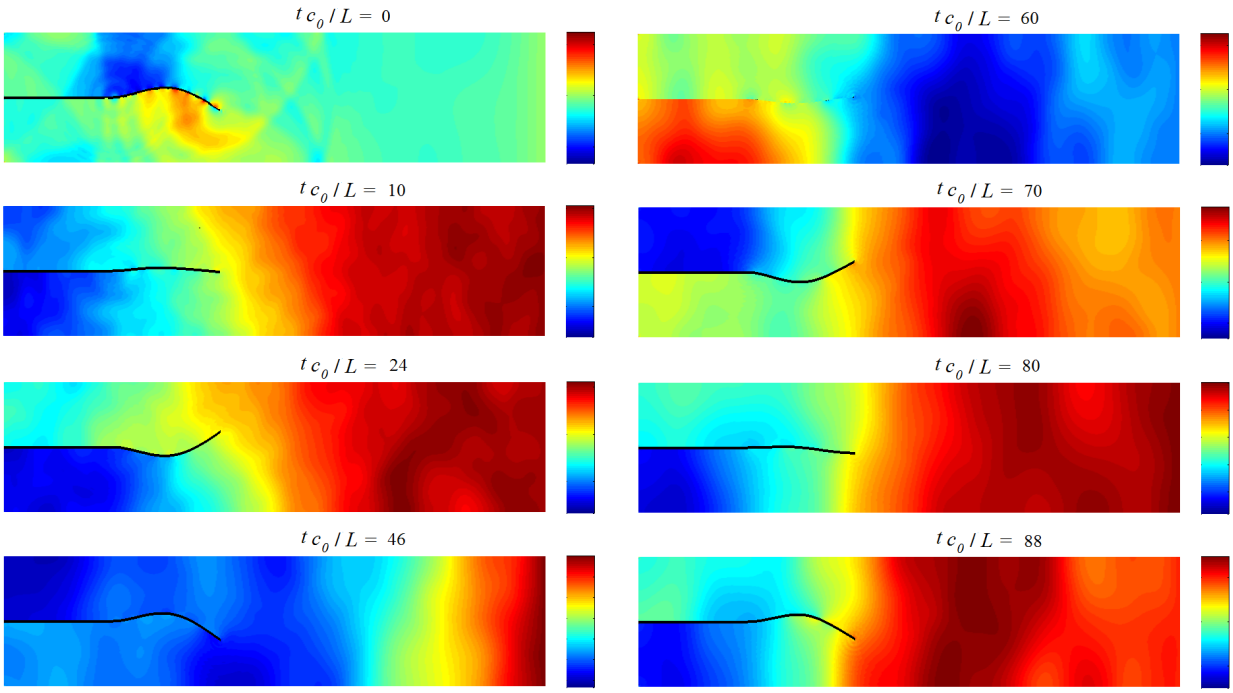

Figure 19: Time sequence showing acoustic pressure contour plots for the first two cycles of oscillation, Re = 378 and Ma = 0.01, the structure data are as in section 3.4, except for the initial tip displacement $\phi(L,0)/H = 0.1$. The outflow pressure is at $p = p_\infty$ and the contour levels are from -3 Pa to 3 Pa corresponding to $-2.48 \times 10^{-3} \leqslant p'/(\rho_0 c_0^2) \leqslant 2.48 \times 10^{-3}$.

Fig. 19 shows the acoustic pressure contours for this simulation. At $tc_0/L = 0$, low and high pressure regions are located over and below the flexible structure, respectively, because the flow there is accelerated and decelerated respectively. When the flexible structure is released at $tc_0/L = 0$, the flow field periodically changes. However, the pressure field is dominated by acoustic waves travelling back and fourth in the channel. As the inlet velocity is fixed, the acoustic pressure waves will be reflected at the inlet. When the acoustic waves hit the outlet, their amplitude will be reduced due to the partly non–reflecting property of Rudy and Strikwerda (1980) boundary treatment, cf. subsection 2.1.2. Thus, the simulated amplitudes of the acoustic pressure waves decrease by interaction with the right boundary. Viscous attenuation contributes to damping of

the acoustic waves. Eventually, the acoustic wave amplitudes decay, which can be observed in Fig. 20.

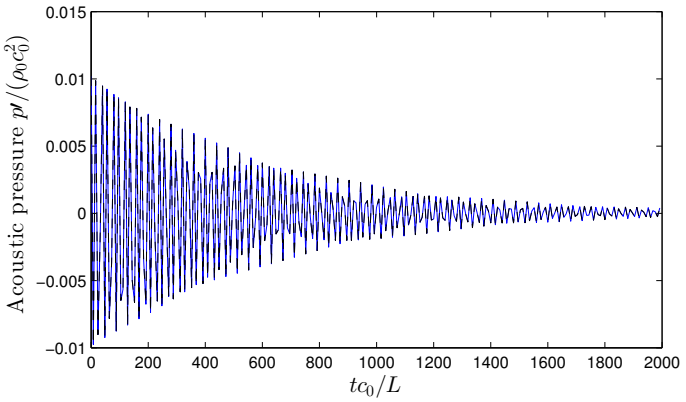

Figure 20: Time history of acoustic pressure $p'/(\rho_0 c_0^2)$ at inlet. The fluid flow is at Re = 378 and Ma = 0.01, the structure data are as in section 3.4, except for the tip displacement $\phi(L,t)/H = 0$ which the plate is a stationary straight splitter.

Therefore, we define a cutoff time $tc_0/L = 2000$ to allow the acoustic pressure to decay. The simulation is repeated with the steady state computation run until $tc_0/L = 2000$. Compared to the previous simulation, the flexible plate is not released from its second mode position with $\phi(L,0)/H = 0.1$ at $tc_0/L = 40$, but at $tc_0/L = 2000$. Fig. 21 illustrates the time history of the acoustic pressure and the frequency of the acoustic pressure spectrum for this simulation. After turning on the fluid–structure interaction at $tc_0/L = 2000$, the frequency of the oscillation of the flexible plate can be observed better due to the decayed acoustic wave amplitudes. Fig. 22 shows the results of the acoustic pressure contours for this simulation.

In Figure 21, a very noisy signal is observed compared to Fig. 18 which is associated with a very complicated behaviour of waves over a long period of time. Since the structure has a curved form, more complex reflections of the pressure waves travel through the computational domain. A plane wave hitting a plate allows reflected waves going out in many directions, hitting the top and bottom walls of the channel. Then these reflected waves interact and make a complex interference pattern which leads to build up a very noisy pressure field. Three acoustic resonance frequencies corresponding to the first three eigenfrequencies of the duct are not as sharp and are more damped compared to those of the previous simulation(cf. Fig. 18) and relatively shifted, particularly high frequencies cf. $f = 600$ Hz (non–dimensional frequencies $f^*_{c_0} = f\frac{L}{c_0} = 0.15$ and $f^*_U = f\frac{L}{U} = 15$) and 1000 Hz ($f^*_{c_0} = 0.25$ and $f^*_U = 25$). The quarter wave mode $f = 200$ Hz ($f^*_{c_0} = 0.05$ and $f^*_U = 5$) is no longer dominant. The fundamental frequency of the soft palate model oscillation $f = 91.5$ Hz ($f^*_{c_0} = 0.022875$ and $f^*_U = 2.2875$) and some harmonics can be observed. The plane waves travelling through the channel change to the circular wave nears the trailing edge (as can be seen in Fig. 19 at $tc_0/L = 0$ and in Fig. 22 at $tc_0/L = 2000$) when the plate starts to oscillate. The resonance frequency $f = 490$ Hz can be identified as a consequence of this phenomenon in both figures 18(b) and 21(b). This acoustic resonance frequency corresponds to the eigenfrequency of each of the two ducts from the inlet to the trailing edge of the flexible plate, i.e., $f = c/(4(L_{\text{rigid plate}} + L_{\text{flexible plate}})) = 500$ Hz ($f^*_{c_0} = 0.125$ and $f^*_U = 12.5$).

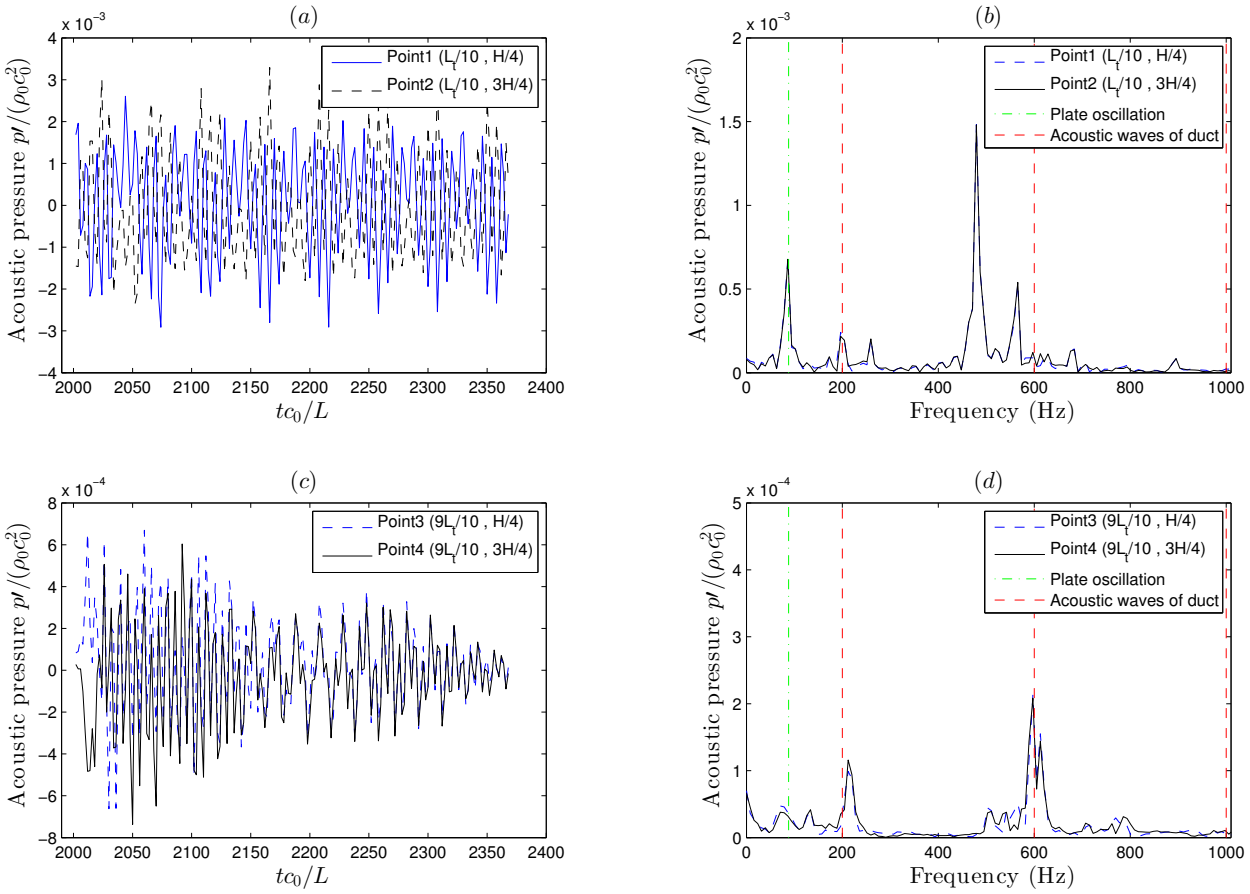

Figure 21: (a) and (c) Time history of acoustic pressure $p'/(\rho_0 c_0^2)$ at inlet and outlet, respectively; (b) and (d) Spectrum of pressure signal. The fluid flow is at Re = 378 and Ma = 0.01, the structure data are as in section 3.4, except for the initial tip displacement $\phi(L,0)/H = 0.1$. The flexible plate was released at $tc_0/L = 2000$.

4. Conclusions

A numerical approach for a simplified model of fluid–structure interaction for the soft palate in the upper airways is developed. This FSI model for the interaction between the inspiratory airflow through nose and mouth with the soft palate has been modeled as compressible viscous flow over a cantilevered flexible plate in a duct. The coupling between the fluid and the structure is handled in an arbitrary Lagrangian–Eulerian (ALE) formulation with an explicit, two–way coupling strategy where forces and deformations are exchanged between the flow and plate at the end of every time step. Strict stability and high order accuracy are obtained by employing summation by parts (SBP) difference operators, which are 6^{th} order accurate in the interior and 3^{rd} order accurate near the boundaries (Svärd and Nordström, 2014). To achieve high accuracy and easy parallelization, the 4^{th} order explicit Runge–Kutta method is applied for time integration. The motion of the cantilevered flexible plate is obtained by solving the linearized Euler–Bernoulli thin beam equation. The numerical method for computing the structure equation is based on the 2^{nd} order central finite difference method and the most accurate and unconditionally stable scheme of

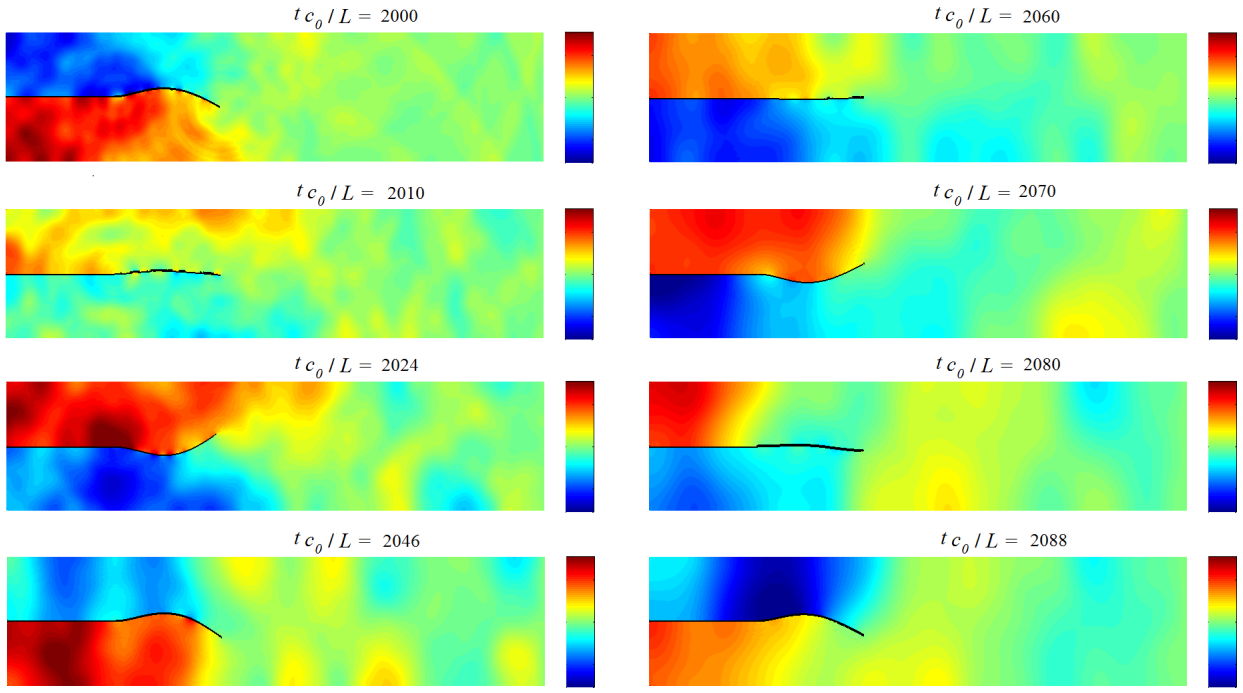

Figure 22: Time sequence showing acoustic pressure contour plots for the first two cycles of oscillation, Re = 378 and Ma = 0.01, the structure data are as in section 3.4, except for the initial tip displacement $\phi(L,0)/H = 0.1$. The outflow pressure is at $p = p_\infty$ and the contour levels are from -3 Pa to 3 Pa corresponding to $-2.48 \times 10^{-3} \leqslant p'/(\rho_0 c_0^2) \leqslant 2.48 \times 10^{-3}$.

the Newmark family.

The dependence of oscillation frequencies of the plate on the grid is studied by varying the number of grid points. The frequencies of plate are compared with the corresponding second mode eigenfrequencies of the structure to assess the required number of grid points. The dynamics of the vortices produced by the interaction of the fluid flow and the structure is investigated when both the upper and lower inlets are open and when only the upper inlet is open the lower one closed. The numerical simulations of FSI show that when both inlets are open the vortices are more stable than when one inlet is closed. Having one inlet closed creates a very complex vortical structure. Several cases are presented to investigate the oscillation behaviour of the flexible plate under different material parameters. For all cases considered, the oscillation of the plate remains stable. The highest rigidity evokes a warning. Close inspection showed that the displacement of the structure developed high wavenumber oscillations. Choosing the time step size for the structure computation twice as large as the time step size for the flow computation, has a stabilizing effect and suppresses the numerical instability. Finally, in order to identify the effect of plate oscillation as a source of sound generation in the evaluation of snoring, the acoustic pressure is analyzed. Although at the given boundary conditions the quarter wave mode is identified as dominant frequency, the frequency of the sound produced by oscillation is in good agreement with the frequency of the plate oscillation. However, the quarter wave frequency and its harmonics dominate the oscillation frequency, as long as the acoustic waves have not yet decayed sufficiently.

5. Acknowledgements

The current research is a part of a larger research project entitled "Modeling of obstructive Sleep apnea by fluid-structure interaction in the upper airways" funded by the Research Council of Norway (Larsson, 2015).

Appendix A. Summation by parts operators

To demonstrate the SBP operators, we apply the procedure to a simplified PDE, that is, rather than analysing the full Navier–Stokes equations in this section, we only focus on the 1D convection–diffusion equation as a model equation.

$$\begin{aligned} &u_t + au_x = bu_{xx}, \quad 0 \le x \le 1 \quad t \ge 0 \\ &u(x,0) = f(x) \\ &u(0,t) = u(1,t) = g(t) = 0 \end{aligned} \tag{A.1}$$

where a and b are assumed to be constant and positive, and u is the dependent variable.

The basis of getting such an energy estimate is to satisfy integration by parts in the discrete sense called Summation–By–Parts (SBP) property (Gustafsson, 2008; Svärd and Nordström, 2014). To outline this technique for model problem (A.1), we consider $u_j = u_j(t)$ the numerical solution of the convection–diffusion equation at grid point $x_j = jh, j = 0, ..., N$, with grid spacing $h = \frac{1}{N}$. The solution vector containing the solution at the discrete grid points is $\mathbf{u} = [u_0(t), u_1(t), ..., u_N(t)]^T$. Using a difference operator Q approximating the first derivative in space, the semi-discrete form of the model equation can be expressed as

$$\frac{d\mathbf{u}}{dt} = -aQ\mathbf{u} + bQQ\mathbf{u}, \quad u_j(0) = f(x_j) \tag{A.2}$$

The discrete scalar product and corresponding norm and energy can be defined by

$$\begin{aligned} &(\mathbf{u}, \mathbf{v})_h = h\mathbf{u}^T H \mathbf{v}, \\ &E_h(t) = \|\mathbf{u}\|_h^2 = (\mathbf{u}, \mathbf{u})_h \end{aligned} \tag{A.3}$$

where H is a diagonal and positive definite matrix defined by $H = \mathrm{diag}(H_L, I, H_R)$. The SBP property is satisfied by the difference operator Q, if

$$(\mathbf{u}, Q\mathbf{v})_h = u_N v_N - u_0 v_0 - (Q\mathbf{u}, \mathbf{v})_h \tag{A.4}$$

or if Q can be written on the form $hQ = H^{-1}P$ for P satisfying

$$P + P^T = E_N - E_0 = \mathrm{diag}(-1, 0, ..., 0, 1) \tag{A.5}$$

where $E_0 = \mathrm{diag}(1, 0, ..., 0)$ and $E_N = \mathrm{diag}(0, 0, ..., 1)$. Using the semi–discrete equation A.2, the energy estimate for the semi–discrete problem can be obtained as

$$\begin{aligned} \frac{dE}{dt} = \frac{d}{dt}\|u(\cdot,t)\|^2 &= (u_t, u)_h + (u, u_t)_h \\ &= (-aQu + bQQu, u)_h + (u, -aQu + bQQu)_h \\ &= -a[u_N^2 - u_0^2] + 2b[u_N(Qu)_N - u_0(Qu)_0] \\ &\quad -2b(Qu, Qu)h \le au_0^2 + 2b[u_N(Qu)_N - u_0(Qu)_0]. \end{aligned} \tag{A.6}$$

We would get non-growing energy in time if the homogeneous boundary conditions could directly be imposed in (A.6). However, this will change the difference operator Q such that its SBP property might be lost. To avoid this problem, boundary conditions are weakly imposed by the simultaneous approximation term (SAT) technique (Gustafsson, 2008). A first derivative SBP operator with diagonal quadrature matrix H in A.3 is a $\mathcal{O}(h^{2s})$ accurate central difference operator which is $\mathcal{O}(h^s)$ accurate at and near boundaries $s = 1, 2, 3$. Such an SBP operator is globally $\mathcal{O}(h^{s+1})$ accurate.

Appendix B. Time step selection

We solve the compressible Navier–Stokes equations explicitly in time. Hence, the time step is restricted by the stability region of the Runge–Kutta method. To analyse the approach for the model (A.1), we consider that the x–derivative is approximated by a standard central p^{th} order finite difference operator $Q_x^{(p)}$ and the time–derivative by an explicit Runge–Kutta method. Therefore, the von Neumann stability analysis leads to the stability condition $\triangle t(-a\hat{Q}^{(p)} + b(\hat{Q}^{(p)})^2) \in S$, where $\hat{Q}^{(p)}$ and S are the Fourier transform of $Q_x^{(p)}$ and the stability domain of the Runge–Kutta method, respectively. The stability condition for SBP operators is more restrictive, due to the requirement $\triangle t \| - aQ_x^{(p)} + bQ_x^{(p)})^2 \|_h \leq R_1 < R$, where the open semicircle $\{z \in \mathbb{C} \mid |z| < R \text{ and } \text{Real}(z) < 0\}$ is contained in the stability domain S (Kreiss and Wu, 1993). For the standard sixth order difference operator, i.e., $(Q_x^{(6)}\mathbf{u})_j = \frac{1}{60\triangle x}(u_{j+3} - 9u_{j+2} + 45u_{j+1} - 45u_{j-1} + 9u_{j-2} - u_{j-3})$, the Fourier transform is $\hat{Q}^{(6)} = \frac{i}{\triangle x}[\frac{3}{2}\sin(k\triangle x) - \frac{3}{10}\sin(2k\triangle x) + \frac{1}{30}\sin(3k\triangle x)]$, where k is the wave number. Thus, the von Neumann stability condition for $Q_x^{(6)}$ and the classical fourth order Runge–Kutta reads $CFL = \frac{|a|\triangle t}{\triangle x} \leq 1.783$ for $b = 0$ and $VNN = \frac{|b|\triangle t}{\triangle x^2} \leq 1.124$ for $a = 0$ (Larsson and Müller, 2009).

References

Auregan, Y., Depollier, C., 1995. Snoring: Linear stability analysis and in-vitro experiments. Journal of Sound and Vibration 188, 39–53.

Balint, T., Lucey, A., 2005. Instability of a cantilevered flexible plate in viscous channel flow. Journal of Fluids and Structures 20, 893–912.

Bertram, C.D., 2008. Flow-induced oscillation of collapsed tubes and airway structures. Respiratory Physiology & Neurobiology 163, 256–265.

Brietzke, S.E., Mair, E.A., 2006. Acoustical analysis of snoring: Can the probability of success be predicted? Otolaryngology-Head and Neck Surgery 135, 417–420.

Guo, C., Païdoussis, M., 2000. Stability of rectangular plates with free side-edges in two-dimensional inviscid channel flow. Journal of Applied Mechanics 67, 171–176.

Gustafsson, B., 2008. High order difference methods for time dependent PDE. Springer, Berlin.

Gustafsson, B., Kreiss, H.O., Oliger, J., 1995. Time dependent problems and difference methods. John Wiley & Sons, New York.

Howell, R., Lucey, A., Carpenter, P., Pitman, M., 2009. Interaction between a cantilevered-free flexible plate and ideal flow. Journal of Fluids and Structures 25, 544–566.

Huang, L., 1995. Flutter of cantilevered plates in axial flow. Journal of Fluids and Structures 9, 127–147.

Huang, L., Zhang, C., 2013. Modal analysis of cantilever plate flutter. Journal of Fluids and Structures 38, 273–289.

Hughes, T.J., 2012. The finite element method: linear static and dynamic finite element analysis. Courier Corporation, New York.

Kreiss, H.O., Wu, L., 1993. On the stability definition of difference approximations for the initial boundary value problem. Applied Numerical Mathematics 12, 213–227.

Kuhl, J.M., DesJardin, P., 2012. Power production locality of bluff body flutter mills using fully coupled 2D direct numerical simulation. Journal of Fluids and Structures 28, 456–472.

Larsson, M., 2015. Welcome to the OSAS page. Http://osas.no/.

Larsson, M., Müller, B., 2009. Numerical simulation of confined pulsating jets in human phonation. Computers & Fluids 38, 1375–1383.

Larsson, M., Müller, B., 2012. High–order numerical simulation of fluid–structure interaction in the human larynx. Progress in Computational Fluid Dynamics, an International Journal 12, 164–175.

Malhotra, A., White, D.P., 2002. Obstructive sleep apnoea. The Lancet 360, 237–245.

Müller, B., 2008. High order numerical simulation of aeolian tones. Computers & Fluids 37, 450–462.

Newmark, N.M., 1959. A method of computation for structural dynamics. Journal of the Engineering Mechanics Division 85, 67–94.

Peyret, R., Viviand, H., Smolderen, J., 1975. Computation of viscous compressible flows based on the Navier-Stokes equations. NASA STI/Recon Technical Report N 76, 11380.

Poinsot, T.J., Lele, S., 1992. Boundary conditions for direct simulations of compressible viscous flows. Journal of Computational Physics 101, 104–129.

Polifke, W., Wall, C., Moin, P., 2006. Partially reflecting and non-reflecting boundary conditions for simulation of compressible viscous flow. Journal of Computational Physics 213, 437–449.

Pulliam, T.H., Steger, J.L., 1980. Implicit finite-difference simulations of three-dimensional compressible flow. AIAA Journal 18, 159–167.

Rudy, D.H., Strikwerda, J.C., 1980. A nonreflecting outflow boundary condition for subsonic Navier-Stokes calculations. Journal of Computational Physics 36, 55–70.

Selle, L., Nicoud, F., Poinsot, T., 2004. Actual impedance of nonreflecting boundary conditions: Implications for computation of resonators. AIAA Journal 42, 958–964.

Sesterhenn, J., Müller, B., Thomann, H., 1999. On the cancellation problem in calculating compressible low Mach number flows. Journal of Computational Physics 151, 597–615.

Shoele, K., Mittal, R., 2016. Flutter instability of a thin flexible plate in a channel. Journal of Fluid Mechanics 786, 29–46.

Strand, B., 1994. Summation by parts for finite difference approximations for d/dx. Journal of Computational Physics 110, 47–67.

Svärd, M., Nordström, J., 2014. Review of summation-by-parts schemes for initial–boundary-value problems. Journal of Computational Physics 268, 17–38.

Tang, L., Païdoussis, M.P., 2007. On the instability and the post-critical behaviour of two-dimensional cantilevered flexible plates in axial flow. Journal of Sound and Vibration 305, 97–115.

Tang, L., Païdoussis, M.P., 2008. The influence of the wake on the stability of cantilevered flexible plates in axial flow. Journal of Sound and Vibration 310, 512–526.

Tetlow, G., Lucey, A.D., 2009. Motions of a cantilevered flexible plate in viscous channel flow driven by a constant pressure drop. Communications in Numerical Methods in Engineering 25, 463–482.

Tian, F.B., Dai, H., Luo, H., Doyle, J.F., Rousseau, B., 2014. Fluid–structure interaction involving large deformations: 3D simulations and applications to biological systems. Journal of Computational Physics 258, 451–469.

Visbal, M.R., Gaitonde, D.V., 2002. On the use of higher-order finite-difference schemes on curvilinear and deforming meshes. Journal of Computational Physics 181, 155–185.

Wu, Y., Cai, X.C., 2014. A fully implicit domain decomposition based ALE framework for three-dimensional fluid–structure interaction with application in blood flow computation. Journal of Computational Physics 258, 524–537.

Young, T., Palta, M., Dempsey, J., Skatrud, J., Weber, S., Badr, S., 1993. The occurrence of sleep-disordered breathing among middle-aged adults. New England Journal of Medicine 328, 1230–1235.